Earthquake Research Advances 2 (2022) 100113

Contents lists available at ScienceDirect

Earthquake Research Advances

journal homepage: www.keaipublishing.com/en/journals/earthquake-research-advances

Rapid report of the 8 January 2022 M_S 6.9 Menyuan earthquake, Qinghai, China

Hongfeng Yang [a,*], Dun Wang [b], Rumeng Guo [c], Mengyu Xie [d], Yang Zang [d], Yue Wang [d], Qiang Yao [b], Chuang Cheng [b], Yanru An [d], Yingying Zhang [d]

[a] Earth System Science Programme, Faculty of Science, The Chinese University of Hong Kong, Shatin, NT, Hong Kong, China
[b] China University of Geosciences Wuhan, Wuhan, Hubei, China
[c] State Key Laboratory of Geodesy and Earth's Dynamic, Innovation Academy for Precision Measurement Science and Technology, Chinese Academy of Sciences, Wuhan, China
[d] China Earthquake Networks Center, China Earthquake Administration, Beijing, China

ARTICLE INFO

Keywords:
Surface rupture
Coseismic slip
Real-time Intensity
Aftershock location and statistics
Earthquake magnitude forecasting

ABSTRACT

The M_S 6.9 Menyuan earthquake in Qinghai Province, west China is the largest earthquake by far in 2022. The earthquake occurs in a tectonically active region, with a background *b*-value of 0.87 within 100 km of the epicenter that we derived from the unified catalog produced by China Earthquake Networks Center since late 2008. Field surveys have revealed surface ruptures extending 22 km along strike, with a maximum ground displacement of 2.1 m. We construct a finite fault model with constraints from InSAR observations, which showed multiple fault segments during the Menyuan earthquake. The major slip asperity is confined within 10 km at depth, with the maximum slip of 3.5 m. Near real-time back-projection results of coseismic radiation indicate a northwest propagating rupture that lasted for ~10 s. Intensity estimates from the back-projection results show up to a Mercalli scale of IX near the ruptured area, consistent with instrumental measurements and the observations from the field surveys. Aftershock locations (up to January 21, 2022) exhibit two segments, extending to ~20 km in depth. The largest one reaches M_S 5.3, locating near the eastern end of the aftershock zone. Although the location and the approximate magnitude of the mainshock had been indicated by previous studies based on paleoearthquake records and seismic gap, as well as estimated stressing rate on faults, significant surface-breaching rupture leads to severe damage of the high-speed railway system, which poses a challenge in accurately assessing earthquake hazards and risks, and thus demands further investigations of the rupture behaviors for crustal earthquakes.

1. Introduction

On January 8, 2022, a strong earthquake with a surface magnitude (M_S) of 6.9 struck the Menyuan county (Fig. 1a), Qinghai Province, northwestern China, shortly after the midnight at the local time of 1:45 a.m. (UTC time 5:45 p.m., January 7). It marked the first major earthquake with magnitude close to 7 in 2022 and was the strongest earthquake in China since the 2021 M_S 7.5 Maduo earthquake that occurred in the same province (Zhan et al., 2021; Guo et al., 2022). The Menyuan earthquake was located at 37.77° N and 101.26° E, with a hypocentral depth of 10 km as reported by the China Earthquake Networks Center (CENC). Immediately after the occurrence of the Menyuan earthquake, emergency response was conducted by different stakeholders. Based on extensive field surveys, the intensity map was announced by China Earthquake Administration (CEA) on January 11, 3 days after the occurrence of the mainshock. The maximum intensity near the epicentral area was IX in the Mercalli scale, and the surface rupture produced by this earthquake was found more than 22 km (https://www.cea.gov.cn/

* Corresponding author.
E-mail address: hyang@cuhk.edu.hk (H. Yang).

Production and Hosting by Elsevier on behalf of KeAi

https://doi.org/10.1016/j.eqrea.2022.100113
Received 16 January 2022; Received in revised form 22 January 2022; Accepted 23 January 2022

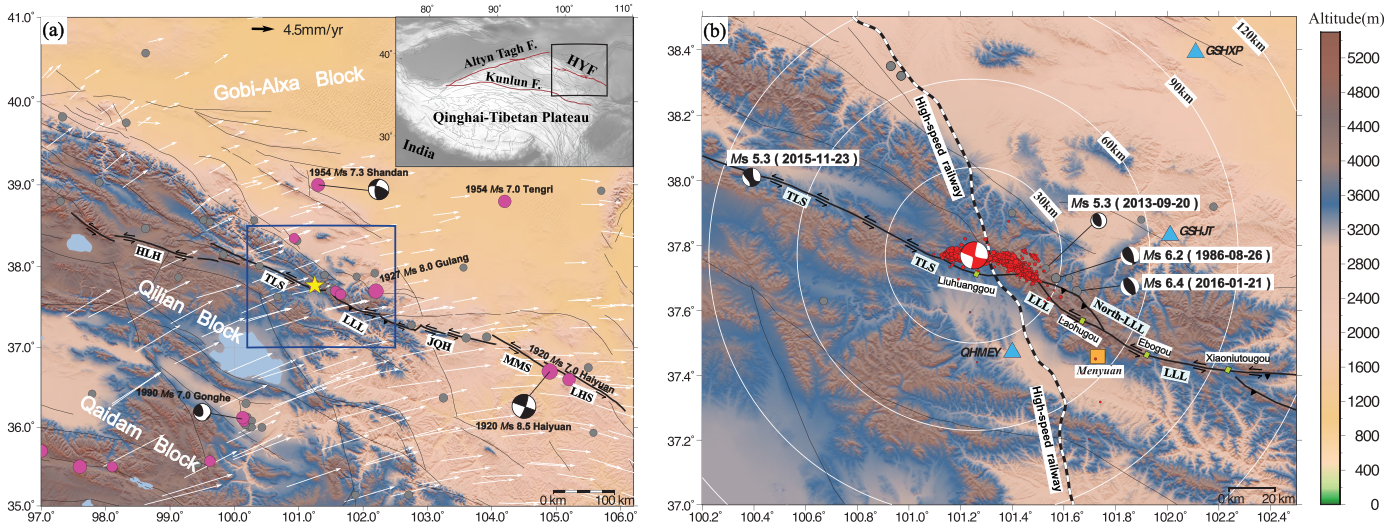

Fig. 1. (a) Major faults (lines), GPS measurements (white arrows), and historical earthquakes (purple and gray dots) in the northeastern margin of the Qinghai-Tibetan Plateau. Yellow star denotes the 2022 M_S 6.9 Menyuan earthquake. LHS: Laohushan fault, MMS: Maomaoshan fault, JQH: Jinqianghe fault, LLL: Lenglongling fault, TLS: Tuolaishan fault, HLH: Hala Lake fault. (b) Focal mechanisms of past and the 2022 earthquakes, aftershock locations (red dots), and seismic stations (blue triangles) in the region. The high-speed railway crosses the rupture zone.

cea/xwzx/fzjzyw/5646200/index.html). The orientation of intensity distribution was northwest-west and the area with intensity no less than VI was 23 417 km^2. Fortunately, the population near the epicenter was few and by far only a few slight injuries have been reported.

The 2022 M_S 6.9 Menyuan earthquake occurred on the Lenglongling fault (LLLF), one segment of the Haiyuan fault zone in the northeastern margin of the Qinghai-Tibetan Plateau, a tectonically active region with numerous large earthquakes. The most recent major event was the 2016 M_S 6.4 Menyuan earthquake (Fig. 1b) that occurred ~40 km to the east of the 2022 epicenter (Fig. 1b). The 2016 earthquake imparted up to 0.4 bar of Coulomb failure stress on the 2022 ruptured plane (Peng et al., 2022), indicating a potential triggering effect. Comparing with previous earthquakes, one striking-feature of the 2022 quake is the massive surface rupture (Fig. 2). Field survey results indicated classical lateral strike-slip motion (Fig. 2c&d), with a maximum ground displacement of ~2.1 m. Echelon cracks (Fig. 2e) on the ground surface and compressional ridges were also identified. The surface rupture crossed one tunnel on the high-speed railway from Lanzhou to Urumuqi (Fig. 2a), leading to severe damage on the Liuhuanggou bridge that was tilted with uneven movements (Fig. 2b).

Immediately after the occurrence of the Menyuan earthquake, rapid post-earthquake products were generated by different research groups, which served as the foundation for emergency response and rescue work, as well as future scientific investigations such as aftershock monitoring and forecasting. To better understand the tectonic setting and mechanism of the 2022 M_S 6.9 Menyuan earthquake, here we introduce a few rapid reports, such as coseismic radiation and slip model, estimated and instrumental record intensity map, aftershock monitoring, location, and relevant statistical results. Similar to preliminary results of previous important earthquakes (e.g. Hardebeck et al., 2004; Han et al., 2018), this rapid report aims at providing timely information of the tectonic environment, responsible fault, and past seismicity in the mainshock source region, which can serve as reference for future investigations of the Menyuan earthquake sequence and the northeastern margin of the Qinghai-Tibetan Plateau.

2. Tectonic settings and past earthquakes

The 2022 M_S 6.9 Menyuan earthquake occurred in the northeastern margin of the Qinghai-Tibetan Plateau, in which numerous faults were formed to accommodate the convergence and material extrusion due to the massive collision between India and Eurasia Plates (Tapponnier et al., 2001). Major fault systems included the Kunlun fault in the south of the margin, the Altyn Tagh fault in the northwest, and the Haiyuan fault (HYF) in the northeast. As a result, a number of damaging earthquakes had occurred in the region, including the great 1920 Haiyuan M 8.5 and 1927 Gulang M 8 earthquakes that were on and adjacent to the HYF (Fig. 1a).

The HYF is indeed one of the most striking fault systems in China, extending over 1000 km from Guyuan, Gansu province in the east to Hala Lake, Qinghai Province in the west (Fig. 1). It consists of a few fault segments, from east to west, the Haiyuan section, Laohushan (LHS), Maomaoshan (MMS), Jinqianghe (JQH), Lenglongling (LLL), Tuolaishan (TLS), and Hala Lake (HLH). The dominant faulting mechanism is strike-slip, with long-term slip rates varying in different segments (Liu et al., 2021).

Near the earthquake is the Lenglongling section (hereafter named LLLF), which was considered to have the highest slip rate (~6.4 mm/yr) along the Haiyuan fault zone (Guo et al., 2017). Previous documentation suggests that at least six historical earthquakes had ruptured the ground based on an analysis of trench samples that were collected in the eastern part of the LLLF (Guo et al., 2019). The average recurrence interval between the six paleo-earthquakes is 1643 ± 568 years (Guo et al., 2019). According to kinematic modeling results with constraints from GPS measurements in the northeastern margin of the Qinghai-Tibetan Plateau (Fig. 3), the maximum shear stress rate of the LLLF is ~ 2 kPa/yr, one of the highest along the HYF (Shi et al., 2018).

On January 23, 2016, an M_S 6.4 earthquake occurred near the central point of the LLLF, leading to numerous landslide and property damages. The distance between the 2016 epicenter and the 2022 earthquake was ~40 km. Based on aftershock relocation and satellite-observed ground deformation, the 2016 Menyuan earthquake was confirmed to be originated from the northern LLLF (Hu et al., 2016; Liu et al., 2019), a branch from the main strand with thrust faulting mechanism, consistent with the moment tensor solutions of the 2016 event (Fig. 1b). In 1986 and 2013, two other thrust earthquakes also occurred in the region, respectively, likely on the northern LLLF as well (Fig. 1b).

3. Mainshock slip distribution

We obtained the coseismic deformation field of the 2022 Menyuan earthquake by using 2 pairs of SAR data from both the ascending (path

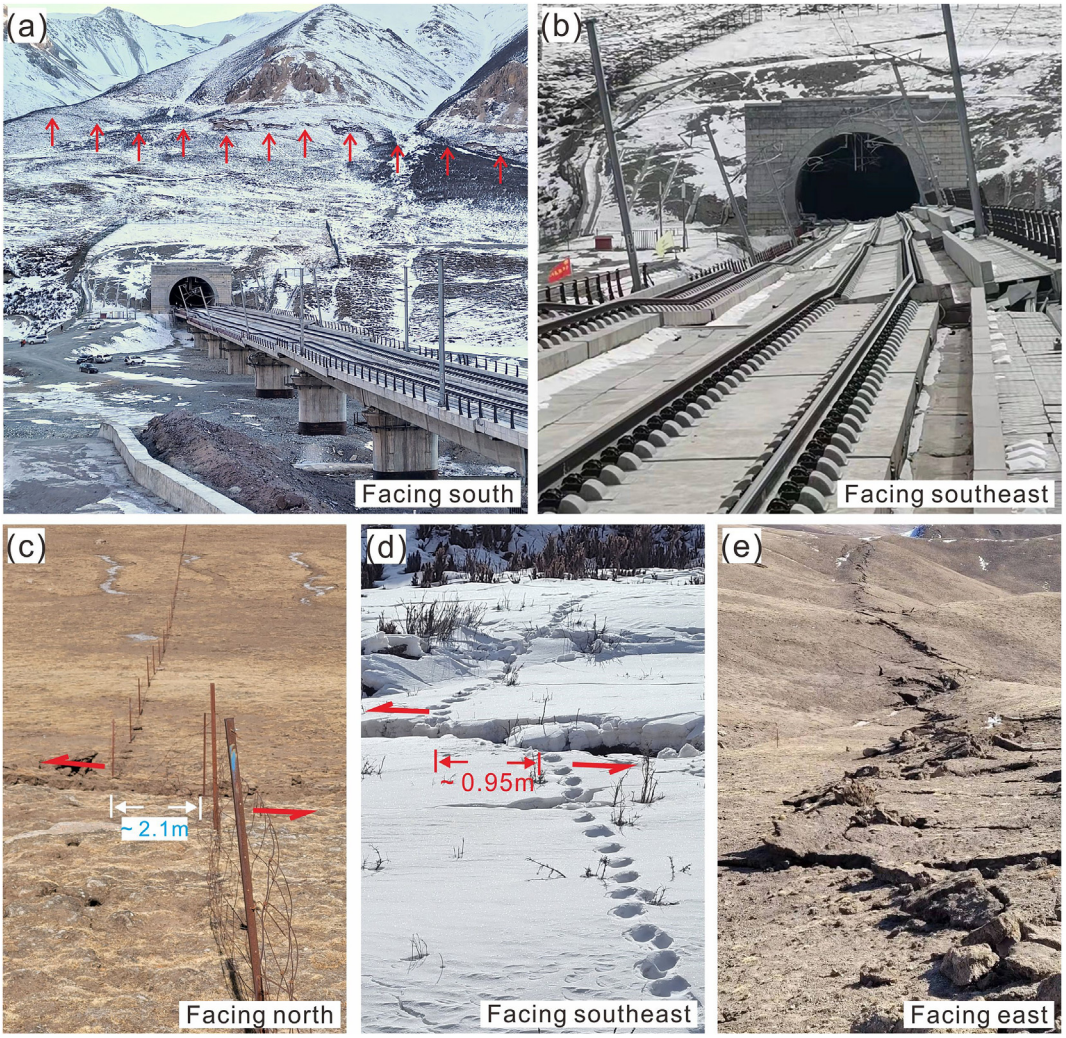

Fig. 2. (a) A field photo showing surface ruptures (red arrows) crossing the tunnel of the high-speed railway associated with the 2022 M_S 6.9 mainshock (Photo credit: Daoyang Yuan @ Lanzhou University). (b) A field photo showing distorted high-speed railways. Photo credit: Jie Gao@China Earthquake Disaster Prevention Center. (c) A fence with an offset of 2.1 m, (d) Footprint traces of animals with an offset of 0.95 m. (e) Echelon structure of the surface rupture. Photo credit: Daoyang Yuan @ Lanzhou University. Courtesy to Han Chen from The Chinese University of Hong Kong.

26, 20211229 - 20220110) and descending (path 33, 20211229 - 20220110) orbits of the Sentinel-1 satellite. The GAMMA commercial software platform was used to process the InSAR data (Werner et al., 2000). To obtain the InSAR coseismic differential interferograms (Fig. 4a), we first simulated the topographic contribution to the radar phase based on the SRTMGL1 DEM with a 30-m spatial resolution (released by NASA) and then eliminated the topographic effects. The interferograms were multi-looked with a factor of 10:2 and filtered using a weighted power spectrum filter (Goldstein et al., 1998) to improve the coherence. We then unwrapped the phase of the differential interferograms based on the minimum cost flow algorithm (Costantini et al., 1998), in which the starting points of unwrapping were selected at stable points away from the epicenter. The atmospheric phase delay error was estimated and removed based on the terrain correlation method. Finally, the unwrapping phases were transformed according to the SAR satellite parameters to obtain the coseismic deformation field in line of sight (LOS) direction of the ascending and descending data (Fig. 4c).

We applied the steepest descent method (Guo et al., 2022) to invert the slip distribution of the Menyuan earthquake. During the inversion, we set all fault planes to extend to the Earth's surface. The refined surface traces of seismogenic faults had been well mapped by the amplitude pixel offsets of SAR image pairs, which were further smoothed to shape the top edges of our preferred fault model. Dip angles were uniformly assumed as 82°. The maximum depth of the fault was set to 20 km, and all fault planes were discretized into rectangular meshes of 2 × 2 km in size. The coseismic observations, model predictions, and their residuals displayed a satisfactory fitting pattern (Fig. 4c). The optimal slip distribution (Fig. 4b) produced a released seismic moment of ~1.3×10^{19} N·m, equivalent to an M_W 6.7 event. Our model had a significant portion of surface-breaching rupture (~20 km), consistent with the findings in field surveys (22 km). The main slip asperity was concentrated at 0–10 km depth, with a maximum slip of ~3.5 m, and the secondary fault segment extending to the west had an average slip of ~0.3 m (Fig. 4b). In contrast, a single planar fault model that was constrained from teleseismic waves suggested a secondary buried slip patch to the east (Peng et al., 2022), which was probably a result of trade-off from teleseismic waves on a simplistic fault geometry.

4. Rupture propagation of the mainshock

We also derived coseismic radiation of the Menyuan mainshock using the back-projection method. Details of the procedure had been described in Wang et al. (2016) and here we only briefly introduced the progress. We used seismic data recorded at the European Virtual Broadband Seismic Network (Fig. 5b). The ranges of azimuths and epicentral distances were 296°–333° and 40°–84°, respectively.

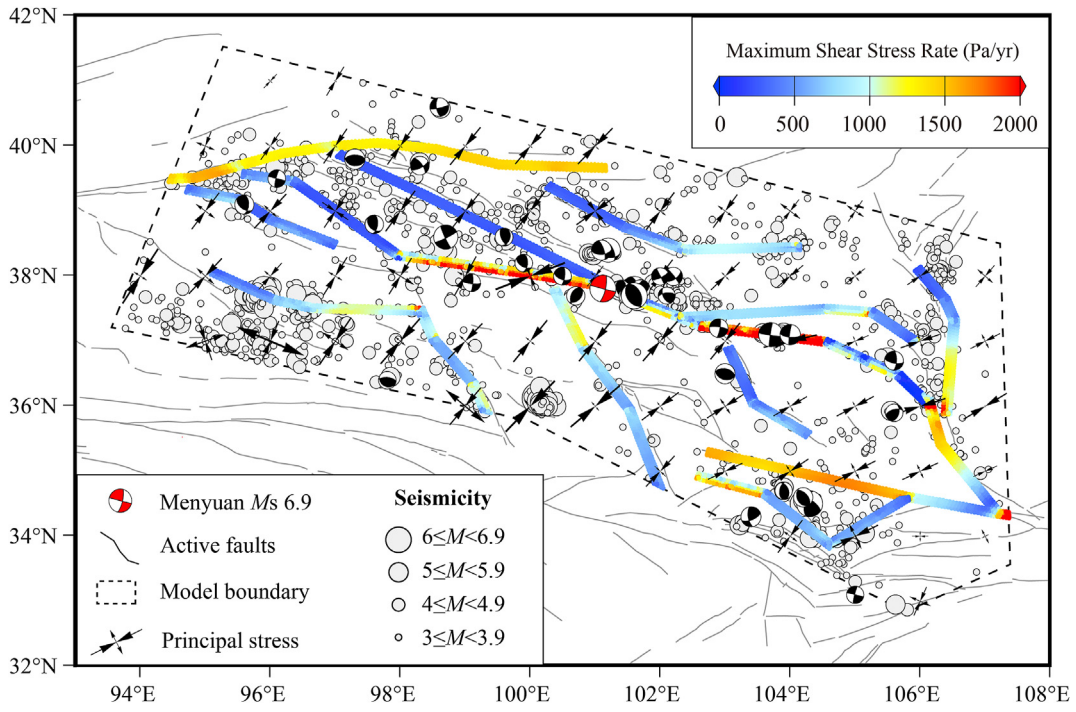

Fig. 3. Shear stress rate in the northeast margin of the Qinghai-Tibetan Plateau derived from finite element modeling with constraints of GPS measurements. Focal mechanisms show past earthquakes in the region. Red ball indicates the location of the 2022 M_S 6.9 Menyuan earthquake. Modified from Shi et al. (2018). Courtesy to Fuqiang Shi from Sha'anxi Earthquake Agency.

We established a grid with 300 × 300 points (horizontal spacing of 1 km at the depth of 10 km) that covered areas with strong ground-shaking. The length of the stacking window was 6 s. We back-projected seismic waveforms that were filtered at two frequency bands of 0.8–8.0 Hz and 1.0–10.0 Hz, respectively. Other parameters were adopted and kept the same to the ones described in Wang et al. (2016).

Fig. 5 showed the spatial distribution of coseismic energy released during the Menyuan earthquake. The earthquake rupture propagated towards NWW for approximately 10–20 km in 10–15 s. The lineation of the ruptured fault was generally compatible with the location pattern of the aftershocks that occurred within two days following the mainshock (Fan et al., 2022). Due to the relatively small magnitude (M_W 6.7), the later part of the back-projected energy points was not well resolved, as evidenced by scattered distributions of the back-projected results 10 s after the origin time.

5. Estimated and instrumental recorded intensity

Furthermore, we estimated the intensity of the Menyuan earthquake in nearly real time from a combination of array technology, multi-source Ground Motion Prediction Equation (GMPE), and site corrections (Chen et al., 2021, 2022). The method involved three steps: estimation of source energy radiation, calculations of PGV according to GMPEs, and site corrections.

We first estimated the fault geometry and rupture directivity from the above back-projection analysis. We then calculated the ground motions using the GMPEs proposed by Si and Midorikawa (1999) that employed the closest distance from a seismic fault to the calculation site and thus only utilized the imaged fault geometry to calculate the ground motion. The PGVs on the ground surface were estimated based on the information about the average shear-wave velocity in the 30 m below the surface (Vs30). Here the value of V_{S30} = 600 m/s was adopted for stiff ground (Si and Midorikawa, 1999).

Following the above steps, the PGV for each site was estimated. According to the China seismic intensity scale (GB/T 17742——2020), we then converted the site corrected PGVs to obtain a seismic intensity map (Fig. 6). The highest intensity (Ⅷ or above) areas were concentrated in the vicinity and northwest of the epicenter. The largest intensity scale was Ⅸ, with a long axis of 32 km and a short axis of 7.5 km, covering an area of about 182 km^2. The long axis of the degree Ⅷ area was 46 km and the short axis was 21 km, covering an area of about 1 448 km^2. The near-real-time back-projection based intensity assessment results showed high similarity with the field survey results that were officially released by CEA on January 11, 2022.

In addition to the estimated intensity based on back-projection results, near the earthquake epicenter there were instrumental records, showing the largest value of 8.2 with an epicentral distance of >10 km (Fig. 7a). The maximum value of the recorded peak ground acceleration was ~457 cm/s^2 (Fig. 7b). The instruments were deployed during the National Project of Earthquake Intensity Rapid Report and Early Warning, based on which the latest Intensity Table was established in 2020 (GB/T 177422020).

6. Aftershock location and monitoring

A large number of aftershocks had been recorded including 7 events with magnitude larger than 4.0. The largest aftershock by far occurred on 6:20 p.m., January 12, with a surface-wave magnitude of 5.3. We conducted double-difference relocations (Waldhasuer and Ellsworth, 2000) of aftershocks in the CENC catalog using network phase picks of P and S waves. After relocation, the aftershocks were distributed along two segments, following the mapped fault traces along the LLLF and TLSF, extending over 40 km along strike (Fig. 8a). The aftershocks extended to ~20 km in depth with steep dip angles on both segments (Fig. 8d and e), similar to other relocation results (Fan et al., 2022; Xu et al., 2022). Early aftershocks were mostly concentrated on the western segment (Fig. 8a). More recent aftershocks, including the M_S 5.3 event, occurred near the eastern end of the aftershock zone (Fig. 8a). There appeared to be an aftershock cluster delineating a potential secondary fault that is nearly parallel to western segment on the LLLF (Fig. 8a&e), which was not found in early (~ 3-4 days post the mainshock) aftershock locations (Fan et al., 2022; Xu et al., 2022).

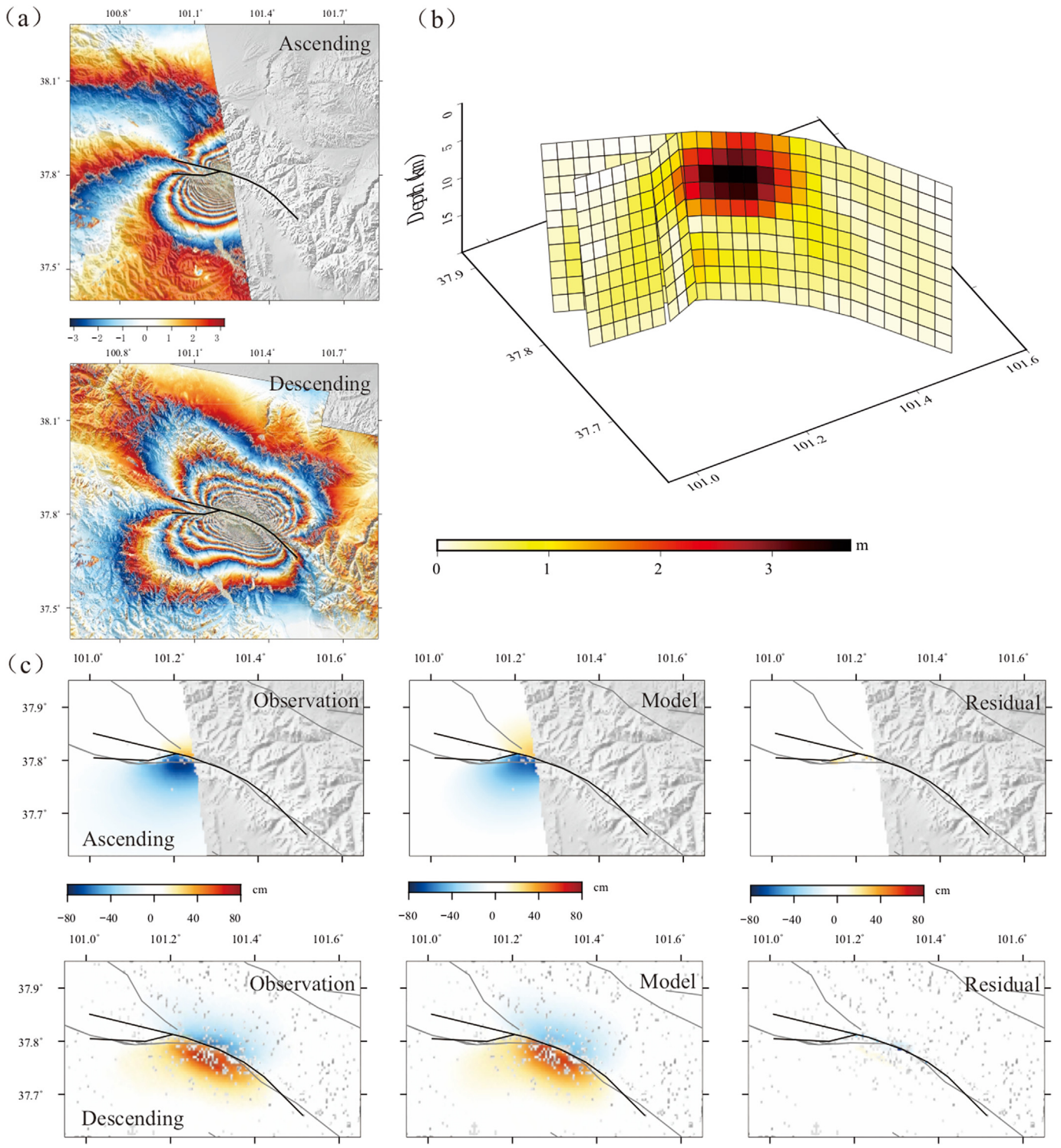

Fig. 4. (a) Coseismic ascending and descending interferograms from InSAR. (b) The coseismic slip distribution of the 2022 Menyuan mainshock. (c) Simulation results of the distributed-slip model. The first and second columns represent the observed and model predictions of InSAR displacements, respectively, and the third column indicates their residuals.

Shortly after the mainshock, a team from Qinghai Earthquake Agency and University of Science and Technology of China had deployed 12 short-period three-component seismometers near the epicenter to monitor aftershocks. The instruments can transfer data in real time and have been proven very effective in the 2021 M_S 6.4 Yangbi and 2021 M_S 7.4 Maduo earthquakes (Li et al., 2021). From the recorded data, earthquake catalog had been constructed in real time using machine-learning phase pickers. Most earthquakes occurred near the LLLF (Fig. 9), similar to our relocations of the network catalog (Fig. 8). However, there were more seismicity in the south of the rupture plane (Fig. 9), which might be attributed to station distribution and detection threshold.

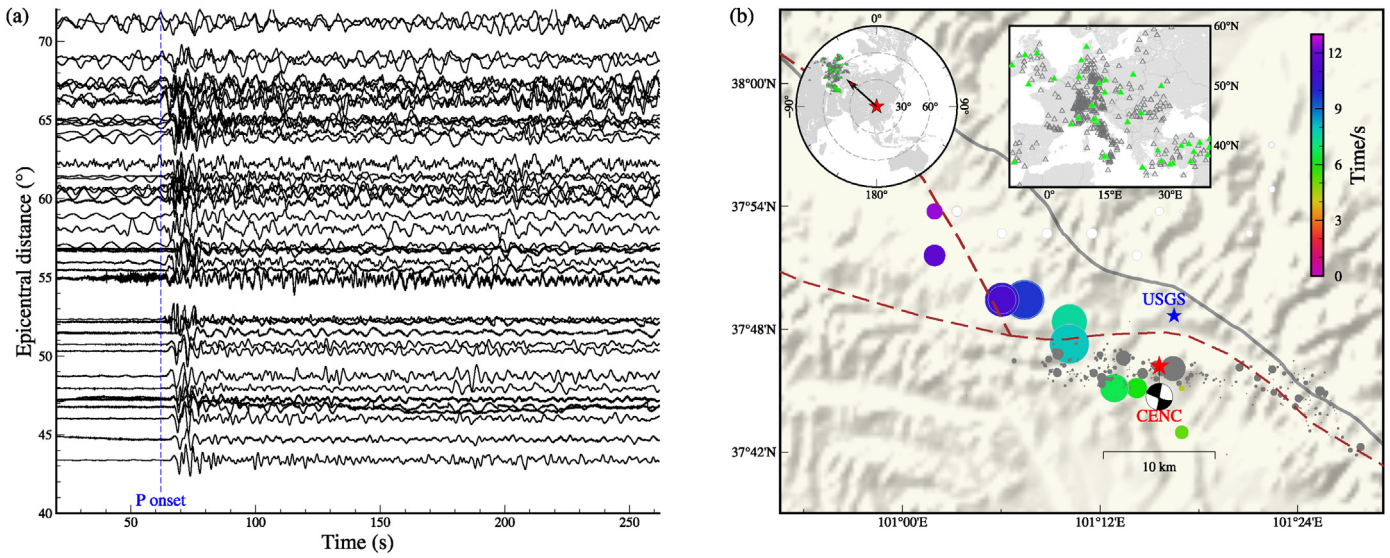

Fig. 5. (a) Waveform records at the European Virtual Broadband Seismic Network, aligned with arrival times of P waves. (b) Timing (color of circles) and amplitude (size of circles) for the stack with the maximum correlation at each time step in the map view. Red and blue stars represent the epicenter of the 2022 M_S 6.9 Menyuan earthquake determined by the CENC and USGS, respectively. Gray circles indicate the locations of aftershocks that occurred within one day following the main shock (from Dr. Lihua Fang). Red lines represent traces of faults. The focal mechanism is from the GCMT. Inset figure shows the locations of stations.

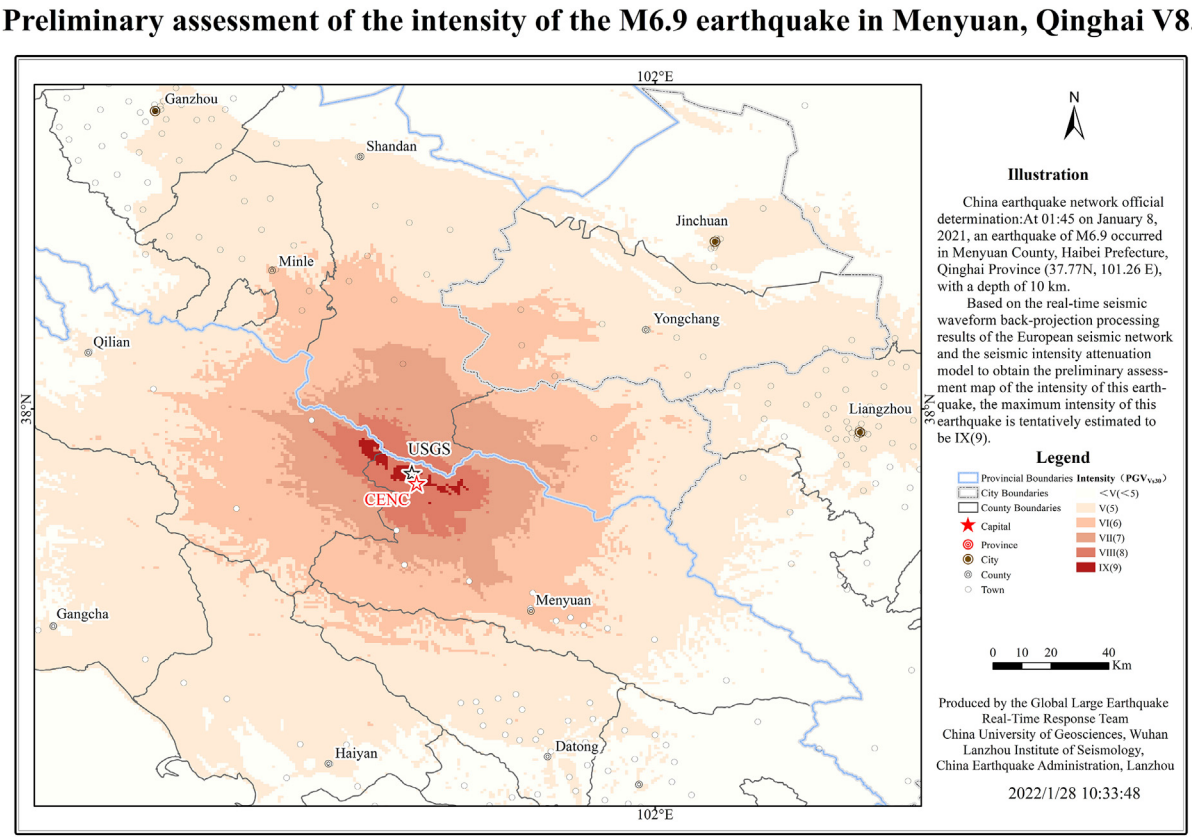

Fig. 6. Preliminary seismic intensity map of the 2022 M_S 6.9 Menyuan earthquake derived from back-projection results. Stars represent epicenters reported by CENC and USGS.

7. Background and aftershock *b* values

After the occurrence of the M_S 6.9 Menyuan earthquake, one practical and important task is to determine whether there might be strong earthquakes, including aftershocks in a short term. A commonly used approach is to derive some statistical parameters of the earthquake sequence, such as *b*-value, and compare with the background one or those in the literature.

We first calculated the background *b*-value and the magnitude completeness (M_c), using the CENC unified catalog from January 1, 2009 to January 7, 2022. The M_c and *b*-value were both calculated at each grid node with an interval of 50 km × 50 km. For each grid node, we selected the closet N earthquakes (Tormann et al., 2014), $N \geq N_{min} = 500$ for calculation. Moreover, we set two limiting conditions. First, we only sampled N events within the maximum radius, $R_{max} = 150$ km of the grid

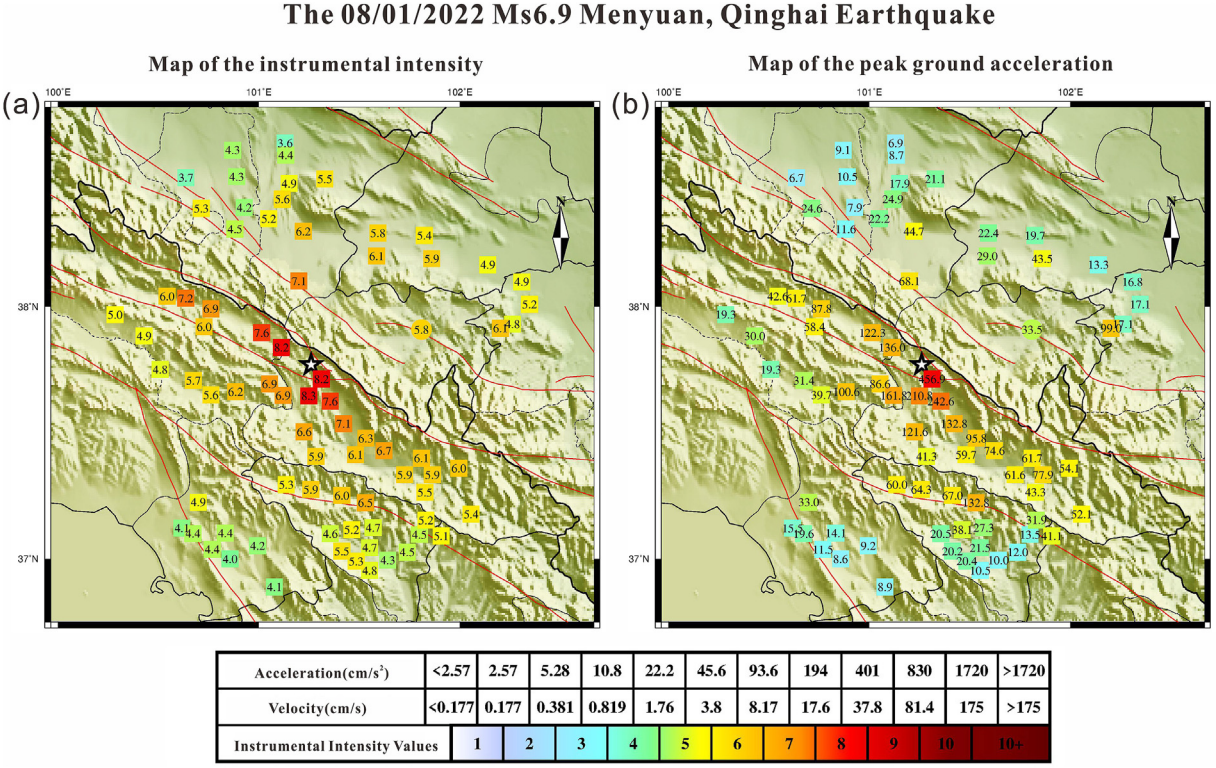

Fig. 7. Intensity (a) and Peak Ground Acceleration (b) measured by nearby strong-motion stations. Courtesy to Strong Motion Observation Group in Institute of Engineering and Mechanics, China Earthquake Administration.

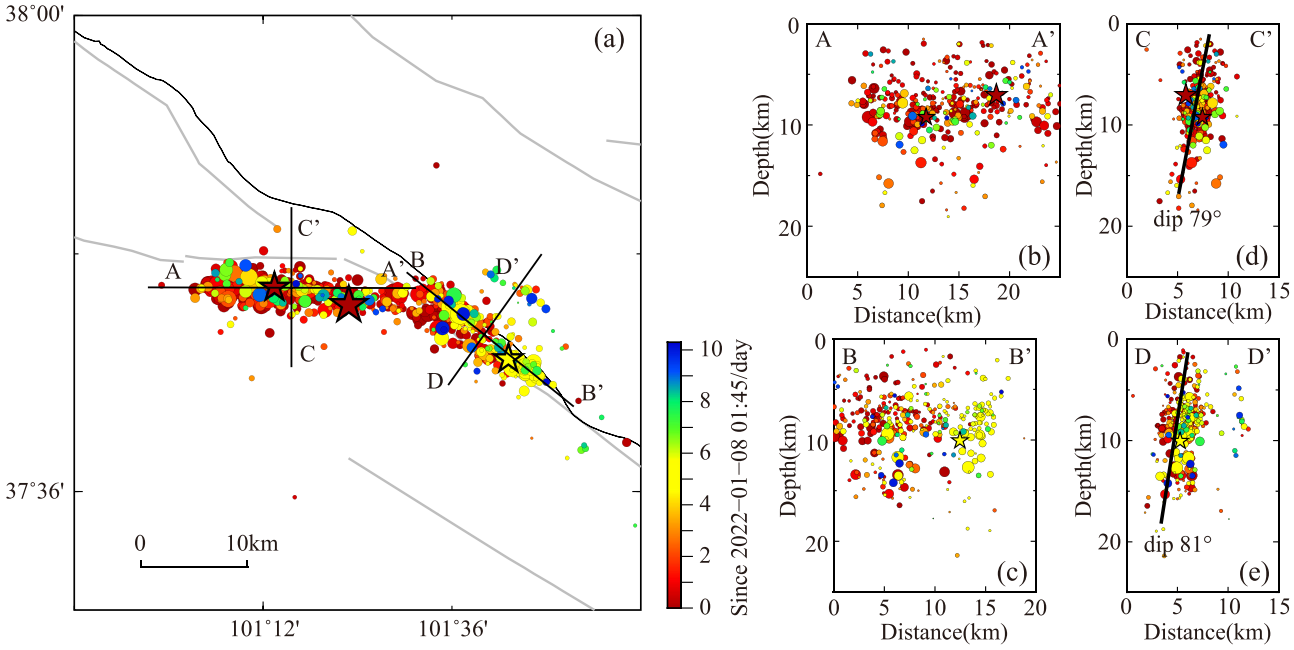

Fig. 8. Relocated aftershocks in the CENC catalog. Map view (a) and cross sections along different profiles (b–e). Color represents the time since the mainshock. Stars denote earthquakes with magnitudes larger than 5.

node. Second, we required that there was at least one earthquake within the minimum radius of the grid node ($R_{min} = 50$ km). To calculate M_c, we use the ZMAP software (Wiemer, 2001), in which the Goodness-of-Fit test (GFT) and Maximum Curvature technique (MAXC) are adopted. We first found M_c when the good-of-fit reached 95% level. Otherwise, we chose 90% level as a compromise. If the 90% level cannot be reached, the M_c was estimated by MAXC with a correction of 0.2 (Woessner and Wiemer, 2005). The *b*-value is estimated by using the maximum-likelihood method when there were at least 50 events above M_c at each grid node.

Both the *b* values and M_c in western China exhibited clear spatial variation. The M_c along the south-north seismic belt was typically lower than 2.0 (Fig. 10a), owing to improved station coverage in recent years. The *b*-value, however, changed rather significantly along the south-north seismic belt (Fig. 10b). The average *b*-value near the 2022 Menyuan earthquake was 0.84, slightly below 1, and the M_c was around 1.6 (Fig. 10).

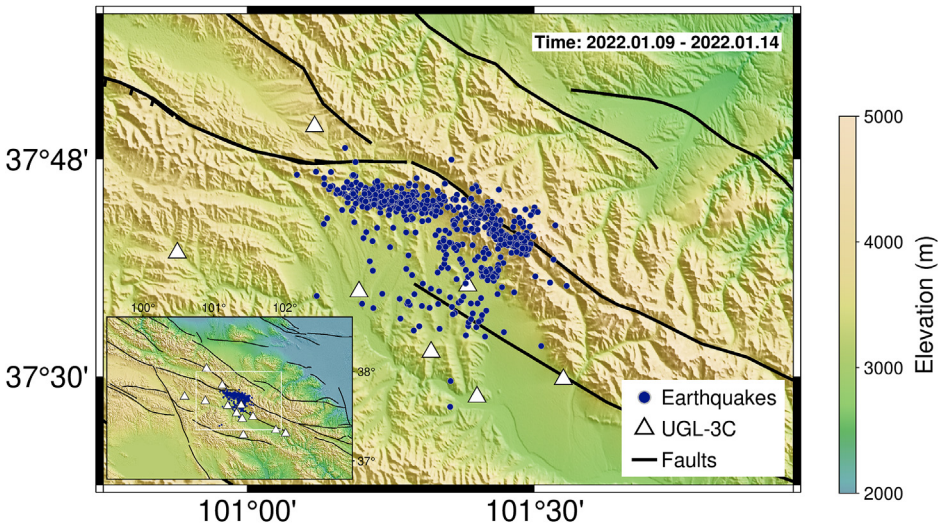

Fig. 9. Rapidly deployed temporary network using real-time data transferring short-period seismometers (white triangles) and machine-learning based aftershock locations (blue dots). Courtesy to Junlun Li from University of Science and Technology of China.

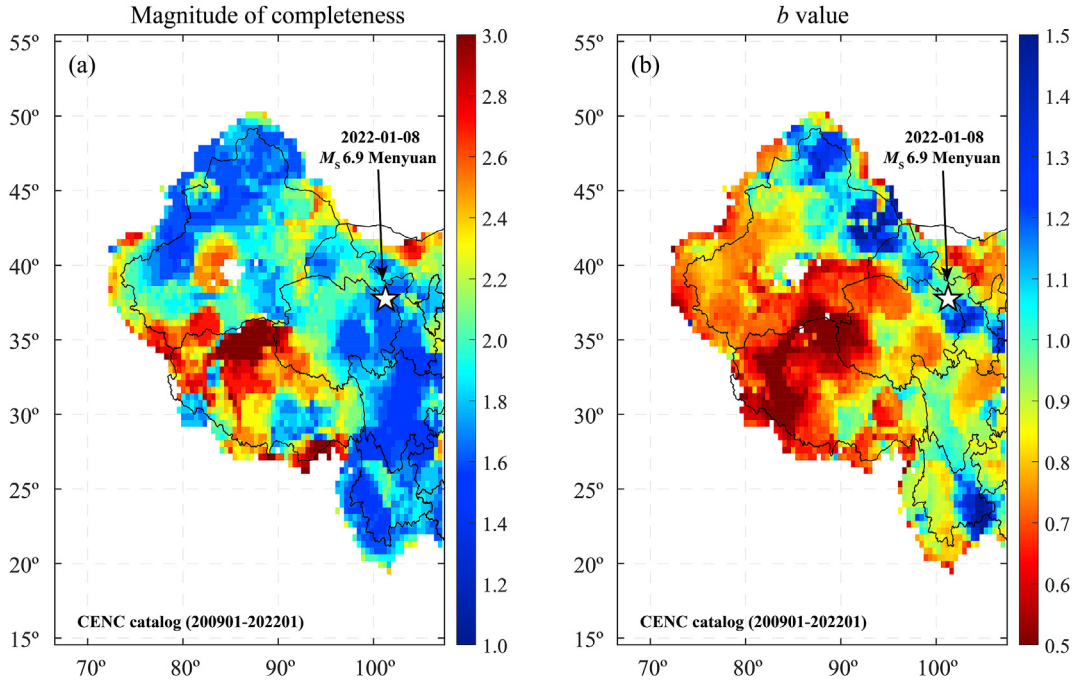

Fig. 10. Magnitude completeness (a) and *b*-value (b) in western China calculated from the China Earthquake Networks Center Catalog (200901-202201). The white star marks the 2022 M_S 6.9 Menyuan earthquake.

In addition to the background *b*-value, we derived the *b*-value for our relocated aftershock sequence till January 21, 2022 (Fig. 11 a&c). The least squared best-fit results showed a value of 0.67, lower than the previous background value. It had been suggested that the temporal *b*-value variation may serve as an indicator to determine whether one earthquake sequence represented ongoing foreshocks or aftershocks (Gulia and Wiemer, 2019). Based on such a decrease of 20% in *b*-value, it would trigger a "foreshock" alarm (Gulia and Wiemer, 2019). However, such a claim must be made on the reliable calculation of the *b* value, which was subject to appropriate choice of seismicity areas and model parameters (e.g. Gulia and Wiemer, 2021; Dascher-Cousineau et al., 2020). To verify, we also calculated the *b*-value of the aftershock sequence using the maximum-likelihood method, which led to an increase in *b*-value shortly after the mainshock, and then variation over time (Fig. 11d). The average value was clearly larger than what was obtained from the least squared method (Fig. 11d).

Apparently, to draw a robust conclusion of whether this may reflect an aftershock or foreshock sequence demanded robust estimation of the *b*-value. Immediately after a major earthquake, calculating the *b*- value faced the challenge of catalog incompleteness and its fluctuation with time. More reliable estimator such as "B-positive" (van der Elst, 2021) can be implemented to improvement the robustness so as to ensure the results, which can be used during the decision process.

8. *H*-value of the Menyuan earthquake sequence

In addition to the *b*-value, we also calculated the *h*-value of this sequence. Mogi (1962) proposed a revised form of the Omori's law to describe the number of aftershocks on the t^{th} day after the mainshock

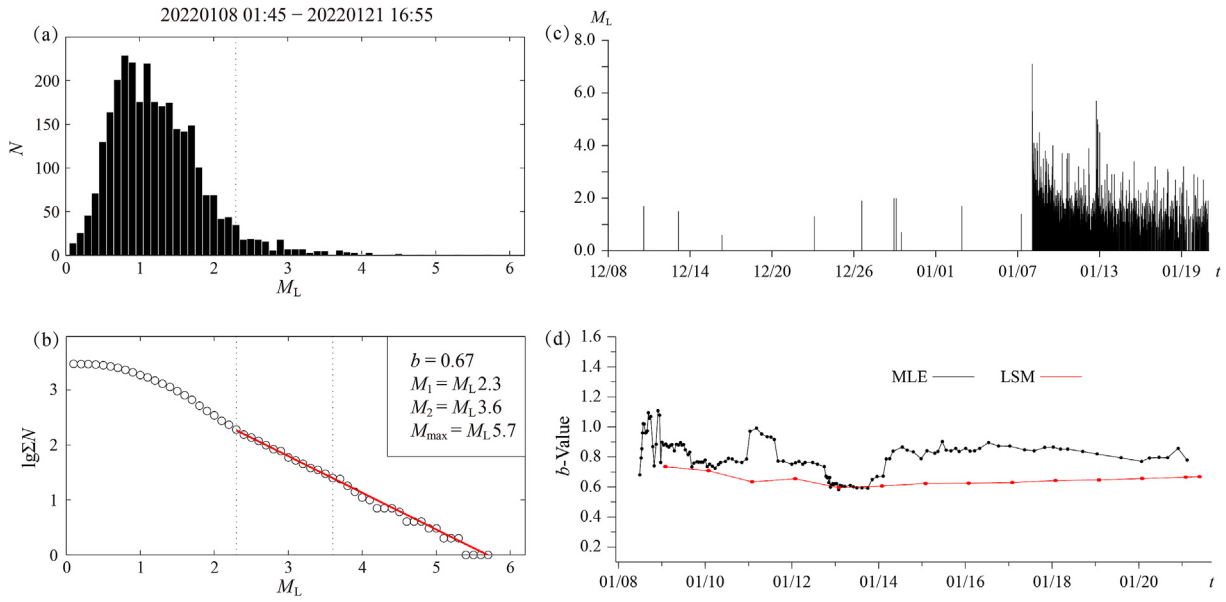

Fig. 11. (a) Magnitude distribution of the aftershocks of the 2022 M_S 6.9 Menyuan earthquake. (b) *b*-value calculated using the least squared method within the magnitude range of M_1 and M_2 (dashed lines). Red line indicates the best-fit model that is used to predict the maximum magnitude (M_{max}), (c) Magnitude distribution over time of the 2022 Menyuan earthquake sequence, one month before and two weeks after the mainshock, (d) temporal variation of *b*-value of the Menyuan aftershock sequence (till January 21, 2022). MLE: maximum likelihood method; LSM: least squared method.

$$N(t) = n_1 t^{-h}, \quad (1)$$

where n_1 and h are constants. By integrating the above equation with the Gutenberg-Richter law, Liu et al. (1979) suggested that the *h*-value can be used to determine whether there might be future events with larger magnitudes during an ongoing sequence. If $h \gg 1$, it indicated that the largest magnitude earthquake already occurred as the mainshock. If $h \approx 1$, additional constraints need to be applied, such as the magnitude difference between the mainshock and the largest aftershock (Liu et al., 1986), in order to evaluate whether future earthquakes with larger magnitudes may occur. If $h \ll 1$, then it was considered as a foreshock sequence.

Our results for the 2022 Menyuan sequence showed that till 8 a.m. on January 21st, the *h*-value of the aftershocks gradually decreased (Fig. 12b). But the overall value was significantly larger than 1 (Fig. 12), suggesting that the Menyuan earthquake sequence is a mainshock-aftershock sequence.

There were also sporadic foreshocks (Fig. 11c) within 40 km of the 2022 mainshock epicenter. The total number of the foreshocks was low and thus the *h*-value was not calculated. For a profound foreshock sequence such as the 2021 M_S 6.4 Yangbi earthquake, Yunnan (Zhang et al., 2022), it may be valuable to test whether the *h*-value can be used to forecast future events with greater magnitudes.

9. Discussion and conclusions

Indeed, multiple lines of evidence suggested that the 2022 Menyuan earthquake was anticipated in its location with the approximate magnitude. Based on paleoearthquake history, fault slip rate, and recognized seismic gap in China, Xu et al. (2017) suggested a few regions that may potentially host surface-breaching earthquakes. The 2022 M_S 6.9 Menyuan earthquake falls in the A3 hazard zone, central segment of the Qilian Mountain that covered nearly 500 km in an east-west aperture (Xu et al., 2017). In addition, shear stress accumulation rate derived from finite element modeling of the northeastern Tibetan plateau with constraints from GPS measurements also indicated that the fault segment ruptured during the 2022 M_S 6.9 Menyuan earthquake is experiencing a high shear stress rate (Shi et al., 2018), thus a potential region for future

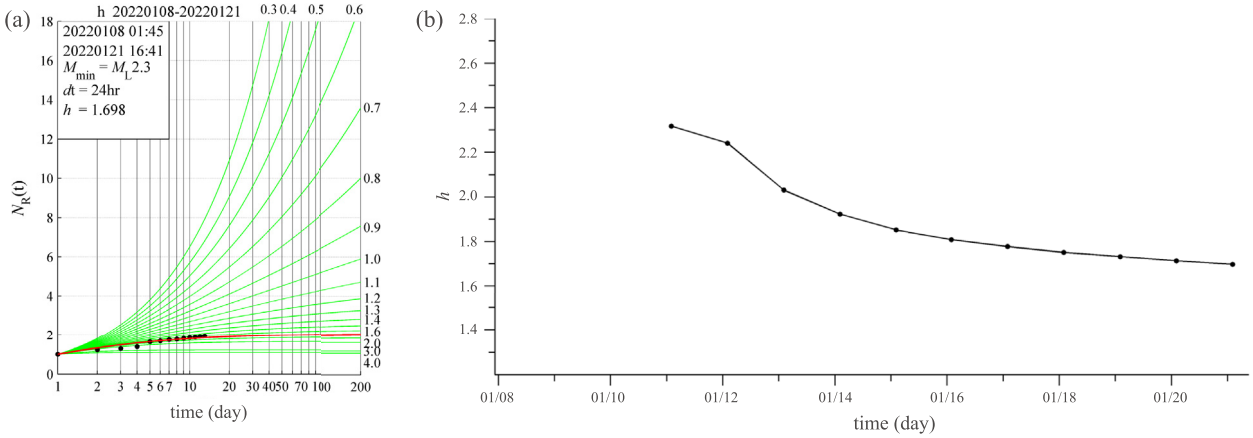

Fig. 12. (a) *h* value (color curves) calculated with a daily time interval for the Menyuan aftershock sequence. Red line shows the best-fit within the time window from January 8 to 21. The minimum magnitude (M_{min}) of aftershocks used was 2.3. (b) Variation of the *h* value with time.

strong earthquakes. Based on slip deficit rate derived from recent GPS measurements, the total slip deficit along the LLLF since the last surface-rupturing earthquake is estimated to be equivalent to a moment magnitude of 7.2 (Zhou et al., 2022). Although it remains unclear how much slip deficit may be released in future earthquakes according to dynamic rupture simulations (Yang et al., 2019; Yao and Yang, 2022), the estimated slip deficit can serve as an upper limit of potentially released seismic moment.

The Menyuan earthquake did not cause any fatality or major injury because of the low population around the epicenter. However, the damage to properties and infrastructures was severe, including the high-speed railway that started service since 2014 (Fig. 2). The primary cause of such severe loss is the surface-breaching rupture that crossed the railway and tunnel (Fig. 2c). Although earthquake ruptures were known to have the potential to break ground given such a magnitude (M_S 6.9 and M_W 6.7) or even smaller (e.g. the 2014 M_W 6.1 Ludian earthquake, Yunnan, China; the 2014 M_W 6.0 Napa Valley earthquake, California, USA), ruptures with similar magnitudes that did not break the ground also exist (e.g. the 2013 M_S 7.0 Lushan and the 2017 M_S 7.0 Jiuzhaigou earthquakes). Clearly, it is critical to evaluate whether a future rupture may reach the ground. Dynamic rupture simulations on a heterogeneous fault show that the surface-breaching rupture and shallow slip highly depend on the hypocentral locations due to the nonlinearity between the rupture radiated energy and the fracture energy on fault (Yao and Yang, 2022). Future work may focus on how to reliably assess the likelihood of ruptures reaching the ground surface, as it plays critical roles in seismic hazard preparation, in particular for the Qinghai-Tibetan Plateau where future railways will be developed as a national strategic plan.

In this paper, we have conducted rapid analysis and present preliminary results of the 2022 M_S 6.9 Menyuan earthquake. Coseismic slip distribution of the mainshock indicates the largest slip of 3.5 -m, with slip extending to the ground along a 20-km long rupture plane, consistent with the findings in the field. Back-projection results suggest rupture propagation predominantly towards the NWW direction. Near real-time intensity maps from back-projection results and instrument records show clear elongation of ground shaking along the NWW direction, consistent with the rupture plane. The maximum intensity is IX, consistent with the official intensity map that was released after extensive field surveys. Aftershock locations exhibit two clear segments, extending to 20 km in depth with estimated dip angles of ~80°. Statistical characteristics of the sequence (b-value and h-value) suggest that the 2022 M_S 6.9 Menyuan earthquake sequence follows the characteristic of mainshock-aftershock sequence.

Declaration of competing interest

The authors declare that they have no known competing financial interests or personal relationships that could have appeared to influence the work reported in this paper.

Acknowledgement

The authors thank a number of scientists who generously shared their results and findings shortly after the earthquake. In particular, we are grateful to Prof. Daoyang Yuan from Lanzhou University, Fuqiang Shi from Sha'anxi Earthquake Agency, Prof. Junlun Li from University of Science and Technology of China, Qiang Ma from Institute of Engineering and Mechanics, CEA, and Han Chen from The Chinese University of Hong Kong, who shared and helped produce figures. The authors thank Zhigang Peng, Ruijia Wang, and an anonymous reviewer who provided timely yet constructive comments. This work is supported by China Earthquake Sciences Experiment Site (2018CSES0102), China Earthquake Administration Science for Earthquake Resilience (XH20072), National Key R & D Program of China (No. 2018YFC0603500), Natural Science Foundation of China (41874062 and 41922025), Youth Science and Technology Fund Project of CENC.

Appendix A. Supplementary data

Supplementary data to this article can be found online at https://doi.org/10.1016/j.eqrea.2022.100113.

References

Chen, W., Wang, D., Zhang, C., Yao, Q., Si, H., 2021. Estimating seismic intensity maps of the 2021 Mw 7.3 Madoi, Qinghai and Mw 6.1 Yangbi, Yunnan, China earthquakes. J. Earth Sci. https://doi.org/10.1007/s12583-021-1586-9, 0-0.

Chen, W., Wang, D., Si, H., 2022. Rapid Estimation of Seismic Intensities Using New Algorithm Incorporating Array Technologies and Ground-Motion Prediction Equations (GMPEs), BSSA (Revison submitted).

Costantini, M., 1998. A novel phase unwrapping method based on network programming. IEEE Trans. Geosci. Rem. Sens. 36, 813–821. https://doi.org/10.1109/36.673674.

Dascher-Cousineau, K., Lay, Thorne, Emily, E. Brodsky, 2020. Reply to "comment on 'two foreshock sequences post gulia and Wiemer (2019)' by Kelian Dascher-Cousineau, Thorne Lay, and Emily E. Brodsky" by Laura gulia and Stefan Wiemer. Seismol Res. Lett. 92 (5), 3259–3264. https://doi.org/10.1785/0220210059.

Fan, L.P., Li, B.R., Liao, S.R., Jiang, C., Fang, L.H., 2022. Precise relocation of the aftershock sequences of the 2022 M6.9 Menyuan earthquake. Earthq. Sci. 35 (3). https://doi.org/10.1016/j.eqs.2022.01.021. In press.

Goldstein, R.M., Werner, C.L., 1998. Radar interferogram filtering for geophysical applications. Geophys. Res. Lett. 25 (21), 4035–4038. https://doi.org/10.1029/1998GL900033.

Gulia, L., Wiemer, S., 2019. Real-time discrimination of earthquake foreshocks and aftershocks. Nature 574 (7777), 193–199.

Gulia, L., Wiemer, S., 2021. Comment on "two foreshock sequences post gulia and Wiemer (2019),". Seismol Res. Lett. https://doi.org/10.1785/0220200428.

Guo, R., Yang, H., Li, Y., Zheng, Y., Zhang, L., 2022. Complex slip distribution of the 2021 Mw 7.4 Maduo, China, earthquake: an event occurring on a slowly slipping fault. Seismol Res. Lett. https://doi.org/10.1785/0220210226.

Guo, P., Han, Z.J., Jiang, W.L., Mao, Z.B., 2017. Holocene left-lateral slip rate of the Lenglongling fault, northeastern margin of the Tibetan Plateau (in Chinese). Seismol. Geol. 39 (2), 323–341. https://doi.org/10.3969/j.issn.0253-4967.2017.02.005.

Guo, P., Han, Z., Mao, Z., Xie, Z., Dong, S., Gao, F., Gai, H., 2019. Paleoearthquakes and rupture behavior of the Lenglongling fault: implications for seismic hazards of the northeastern margin of the Tibetan Plateau. J. Geophys. Res. Solid Earth 124, 1520–1543. https://doi.org/10.1029/2018JB016586.

Han, L., Jia, Cheng, An, Yanru, Fang, Lihua, Jiang, Changsheng, Chen, Bo, Wu, Zhongliang, Liu, Jie, Xu, Xiwei, Liu, Ruifeng, Yao, Zhixiang, Wang, Changzai, Wang, Yushi, 2018. Preliminary report on the 8 august 2017 MsMs 7.0 Jiuzhaigou, Sichuan, China, earthquake. Seismol Res. Lett. 89 (2A), 557–569. https://doi.org/10.1785/0220170158.

Hardebeck, J.L., Boatwright, J., Dreger, D., et al., 2004. Preliminary report on the 22 December 2003, M 6.5 san Simeon, California earthquake. Seismol Res. Lett. 75 (2), 155–172.

Hu, C., Yang, P., Li, Z., et al., 2016. Seismogenic mechanism of the 21 january 2016 Menyuan, Qinghai Ms 6.4 earthquake. Chin. J. Geophys. 59 (5), 1637–1646. https://doi.org/10.6038/cjg20160509 (in Chinese).

Li, Junlun, Yao, Huajian, Wang, Baoshan, Yang, Yang, Hu, Xin, Zhang, Lishu, Ye, Beng, Yang, Jun, Li, Xiaobin, Liu, Feng, Chen, Guoyi, Guo, Chang, Wen, Yang, 2021. A real-time AI-assisted seismic monitoring system based on new nodal stations with 4G telemetry and its application in the Yangbi M6.4 aftershock monitoring in southwest China. Earthquake Res. Adv. https://doi.org/10.1016/j.eqrea.2021.100033.

Liu, J., Ren, Z., Min, W., Ha, G., Lei, J., 2021. The advance in obtaining fault slip rate of strike slip fault-A review. Earthquake Res. Adv. 1 (4). https://doi.org/10.1016/j.eqrea.2021.100032.

Liu, M., Li, H., Peng, Z., Ouyang, L., Ma, Y., Ma, J., Liang, Z., Huang, Y., 2019. Spatial-temporal distribution of early aftershocks following the 2016 Ms 6.4 Menyuan, Qinghai, China Earthquake. Tectonophysics 766, 469–479. https://doi.org/10.1016/j.tecto.2019.06.022.

Liu, Z., Qian, Z., Wang, W., 1979. Decay in earthquake frequency, an indicator of foreshocks. J. Seismo. Res. 2 (4), 1–9 (in Chinese).

Liu, Z., Kong, Z., 1986. Earthquake frequency attenuation and earthquake prediction. J. Seismo. Res. 9 (1), 1–12 (in Chinese).

Mogi, K., 1962. On the Time Distribution of Aftershocks Accompanying the Recent Major Earthquakes in and Near Japan, vol. 40. Bull. Earthquake Res. Inst., Tokyo Univ., pp. 107–124

Si, Midorikawa, 1999. New Attenuation relationships for peak ground acceleration and velocity considering effects of fault type and site condition. J. Struct. Constr. Eng. 523, 63–70.

Peng, Zhigang, Liu-Zeng, Jing, Deng, Yangfan, Toda, Shinji, 2022. Strong earthquake increases seismic hazard in Qinghai, China. Temblor. https://doi.org/10.32858/temblor.230.

Shi, F., Shao, Z., Zhan, W., et al., 2018. Numerical modelling of the shear modulus of stress state of active faults in the northeastern margin of the Tibetan plateau. Chin. J. Geophys. 61 (9), 3651–3663. https://doi.org/10.6038/cjg2018L0631.

Tormann, T., Wiemer, S., Mignan, A., 2014. Systematic survey of high-resolution b value imaging along Californian faults: inference on asperities [J]. J. Geophys. Res. Solid Earth 119, 2029–2054. https://doi.org/10.1002/2013JB010867.

Van der Elst, N., 2021. *B-positive*: a robust estimator of aftershock magnitude distribution in Transiently incomplete catalogs. J. Geophys. Res. https://doi.org/10.1029/2020JB021027.

Waldhauser, F., Ellsworth, W.L., 2000. A double-difference earthquake location algorithm: method and application to the northern Hayward fault, California. Bull. Seismol. Soc. Am. 90 (6), 1353–1368.

Wang, D., Kawakatsu, H., Mori, J., Ali, B., Ren, Z., Shen, X., 2016. Backprojection analyses from four regional arrays for rupture over a curved dipping fault: the Mw 7.7 24 September 2013 Pakistan earthquake. J. Geophys. Res. Solid Earth 121 (3), 1948–1961.

Werner, C., Wegmüller, U., Strozzi, T., Wiesmann, A., 2000. Gamma SAR and interferometric processing software. In: Paper Presented at the Proceedings of the Ers-Envisat Symposium. Gothenburg, Sweden.

Wiemer, S., 2001. A software package to analyze seismicity: ZMAP [j]. Seismol Res. Lett. 72 (3), 373–382. https://doi.org/10.1785/gssrl.72.3.373.

Woessner, J., Wiemer, S., 2005. Assessing the quality of earthquake Catalogues: estimating the magnitude of completeness and its uncertainty [J]. Bull. Seismol. Soc. Am. 95 (2), 684–698. https://doi.org/10.1785/0120040007.

Xu, Y.C., Guo, X.Y., Feng, L.L., 2022. Relocation and focal mechanism solutions of the MS6.9 Menyuan earthquake sequence on January 8, 2022 in Qinghai Province. Acta Seismol. Sin. 44 (2). https://doi.org/10.11939/jass.20220008. In press.

Xu, X., Wu, X., Yu, G., Tan, X., Li, K., 2017. Seismo-geological signatures for identifying M $\geq$ 7.0 earthquake risk areas and their premilimary application in mainland China. Seismol. Geol. 39 (2). https://doi.org/10.3969/j.issn.0253-4967.2017.02.001.

Yang, H., Yao, S., He, B., Newman, A.V., 2019. Earthquake rupture dependence on hypocentral location along the Nicoya Peninsula subduction megathrust. Earth Planet Sci. Lett. 520, 10–17. https://doi.org/10.1016/j.epsl.2019.05.030.

Yao, S., Yang, H., 2022. Hypocentral dependent shallow slip distribution and rupture extents along a strike-slip fault. Earth Planet Sci. Lett. 578. https://doi.org/10.1016/j.epsl.2021.117296, 117296, ISSN 0012-821X.

ZHOU, Lin, Ji, Lingyun, Li, Zhangjun, etal, 2022. Study on Current deformation process and seismicity of lenglongling area based on small earthquakes and GPS data[J]. J. Seismol. Res. 45 (1), 1–7. https://doi.org/10.20015/j.cnki.ISSN1000-0666.2022.0017.

Zhan, Y., Liang, M.J., Sun, X.Y., et al., 2021. Deep structure and seismogenic pattern of the 2021.5.22 Madoi (Qinghai) M_S7.4 earthquake. Chin. J. Geophys. 64 (7), 2232–2252. https://doi.org/10.6038/cjg2021O0521.

Zhang, Y., An, Y., Long, F., Zhu, G., Qin, M., Zhong, Y., Xu, Q., Yang, H., 2022. Short-term foreshock and aftershock patterns of the 2021 Ms 6.4 Yangbi earthquake sequence. Seismol Res. Lett. 93 (1), 21–32. https://doi.org/10.1785/0220210154.